

Special  
Collection

# Electrochemical Cleaning Stability and Oxygen Reduction Reaction Activity of 1–2 nm Dendrimer-Encapsulated Au Nanoparticles

Juliette W. Strasser,<sup>[a]</sup> Thomas J. P. Hersbach,<sup>[a]</sup> Jing Liu,<sup>[b]</sup> Aliya S. Lapp,<sup>[a]</sup>  
Anatoly I. Frenkel,<sup>\*,[c, d]</sup> and Richard M. Crooks<sup>\*,[a]</sup>

Here we show that just three electrochemical scans to modest positive potentials result in substantial growth of 1–2 nm Au dendrimer-encapsulated nanoparticles (DENS). We examined two sizes of Au DENS, denoted as G6-NH<sub>2</sub>(Au<sub>147</sub>) and G6-NH<sub>2</sub>(Au<sub>55</sub>), where G6-NH<sub>2</sub> represents a sixth-generation, amine-terminated, poly(amidoamine) dendrimer and the subscripts, 147 and 55, represent the average number of atoms in each size of DENS. *Ex situ* transmission electron microscopy (TEM) and *in situ* X-ray absorption spectroscopy (XAS) results indicate

that G6-NH<sub>2</sub>(Au<sub>55</sub>) DENS grow to the same size as the G6-NH<sub>2</sub>(Au<sub>147</sub>) DENS following these scans. Importantly, this growth occurs prior to the onset of detectable faradaic Au oxidation or reduction current. The observed growth in the size of the DENS directly correlates to changes in the electrocatalytic ORR activity. The key point is that after just three positive scans the G6-NH<sub>2</sub>(Au<sub>147</sub>) and G6-NH<sub>2</sub>(Au<sub>55</sub>) DENS are essentially indistinguishable in terms of both physical and electrocatalytic properties.

## 1. Introduction

In the field of electrocatalysis it is common practice to subject nanoparticles (NPs) to electrochemical processes intended to remove impurities from the catalyst surface.<sup>[1–8]</sup> This is often referred to as 'electrochemical cleaning', and its purpose is to expose a pristine NP surface so that electrocatalytic performance can be accurately assessed.<sup>[9–12]</sup> It is becoming increasingly clear, however, that these types of pretreatments can significantly alter the properties of the catalysts under study. For example, following pretreatment, structured bimetallic NPs can undergo atomic rearrangements,<sup>[13–16]</sup> the crystal structure, shape, and facets can change,<sup>[4,17–19]</sup> and atoms can undergo selective dissolution.<sup>[7,8,13,16,20–22]</sup> Even for polycrystalline gold surfaces, the rate of anodic Au dissolution during potential

cycling is highly dependent on the surface structure of the electrode.<sup>[23]</sup> These atomic-level structural changes are further exacerbated for very small (< ~5 nm) NPs due to their inherent instability.<sup>[24–27]</sup>

The foregoing problems are further compounded by the fact that in some cases electrocatalytic NPs are only characterized immediately after synthesis, less frequently after catalysis, and generally not at all during or after cleaning protocols. Structural changes that might occur during these processes are particularly problematic when theoretical methods are used to predict or rationalize structure-function relationships.<sup>[28–30]</sup> To address these issues, we report herein a quantitative study demonstrating that AuNPs in the 1–2 nm size range undergo size changes during a common electrochemical cleaning protocol. The important result is that these structural changes have significant consequences for subsequent electrocatalytic reactions.

Over the past decade or two, methods for synthesizing and characterizing NPs have become increasingly refined. For example, it is now possible to prepare AuNPs having remarkable structural fidelity.<sup>[31–35]</sup> As NP size decreases, however, their stability also decreases; electrocatalytically active NPs are especially susceptible to such effects.<sup>[27,36,37]</sup> For example, Pattadar and Zamborini showed that ~2 nm AuNPs oxidize at potentials ~250 mV more negative than ~4 nm AuNPs.<sup>[27]</sup> In this same study, it was also found that ~2 nm AuNPs increase in size to ~4 nm after just one cyclic potential scan.<sup>[27]</sup> In fact, it has been demonstrated that AuNPs ranging in initial sizes from 0.8 to 4.5 nm grow to ~5 nm following electrochemical cycling.<sup>[24]</sup> Despite the fact that electrochemical processes leading to NP growth are well established, the impact of electrochemical cleaning on NP growth, and its subsequent effect on electrocatalysis, have not been thoroughly investigated.

[a] J. W. Strasser, Dr. T. J. P. Hersbach, Dr. A. S. Lapp, Prof. R. M. Crooks  
Department of Chemistry and Texas Materials Institute  
The University of Texas at Austin  
2506 Speedway, Stop A5300, Austin, TX 78712-1224, U.S.A.  
E-mail: crooks@cm.utexas.edu

[b] Prof. J. Liu  
Department of Physics  
Manhattan College  
Riverdale, NY 10471, USA

[c] Prof. A. I. Frenkel  
Department of Materials Science and Chemical Engineering  
Stony Brook University  
Stony Brook, NY 11794, USA  
E-mail: anatoly.frenkel@stonybrook.edu

[d] Prof. A. I. Frenkel  
Division of Chemistry  
Brookhaven National Laboratory  
Upton, NY 11973, USA

 Supporting information for this article is available on the WWW under <https://doi.org/10.1002/celec.202100549>

 An invited contribution to a joint Special Collection in memory of Prof. Jean-Michel Savéant.

A number of studies have addressed the effect of AuNP size on the electrochemical oxygen reduction reaction (ORR).<sup>[38–40]</sup> It has generally been found that ORR activity increases as the AuNP size decreases. For example, Chen and Chen reported an inverse relationship between catalytic activity for the ORR in basic solutions and NP size. In this study, the highest activity was observed for Au<sub>11</sub> clusters having a diameter of 0.8 nm.<sup>[39]</sup> Likewise, the activity of AuNPs used for the electrocatalytic CO<sub>2</sub> reduction reaction has also been shown to depend on the size of AuNPs.<sup>[41]</sup>

Theoretical calculations also suggest that smaller AuNPs may exhibit enhanced electrocatalytic activity.<sup>[42,43]</sup> As alluded to earlier, however, accurate correlation of theory and experiment requires knowledge of NP size and structure during electrocatalytic reactions. The best way to do this involves *operando* measurements,<sup>[44–48]</sup> but this is often difficult or impossible to achieve. As an alternative, one can evaluate the size and structure of catalysts before and after electrocatalytic reactions. For example, our group used this approach to show that AuNPs grow from 2 nm prior to electrocatalytic CO<sub>2</sub> reduction to 6 nm afterward.<sup>[25]</sup> In that case, one could definitively conclude that the NPs changed during electrocatalysis. If catalytic NPs retain their original size after reaction, however, it is likely (but not certain) that they did not undergo dramatic structural changes during reaction.<sup>[26,49]</sup>

Dendrimer-encapsulated nanoparticles, or DENs,<sup>[50–52]</sup> are an effective catalytic model for studying the relationship between NP size and catalytic activity.<sup>[6,25,53,54]</sup> The reason for this is twofold. First, the dendrimer serves as a template during synthesis, and therefore the resulting NPs are typically nearly monodisperse in size.<sup>[55]</sup> Second, the dendrimer tends to stabilize NP size during electrocatalytic reactions without itself influencing catalytic sites present on the surface of the encapsulated NP.<sup>[52]</sup> Indeed, we recently reported an example demonstrating the effectiveness of these two factors for studying the stability of AuNPs during the electrochemical CO<sub>2</sub> reduction reaction.<sup>[25]</sup>

In the present report we focus on how electrochemical pretreatment steps; that is, 'electrochemical cleaning', affects the final size of 1–2 nm AuNPs. The results show that Au DENs in this size range grow to an average limiting size of at least ~2 nm. We also show that this change in size impacts catalytic activity, kinetics and electron transfer for the electrocatalytic ORR. In the absence of electrochemical cleaning, however, Au DENs retain their original size even after the ORR. The findings reported here have important consequences for future studies of < 2 nm electrocatalytic NPs.

## Experimental Section

### Chemicals and Materials

All chemicals were used as received unless otherwise noted. Sixth-generation poly(amidoamine) (PAMAM) dendrimers (G6-NH<sub>2</sub>) were purchased from Dendritech, Inc. (Midland, MI) as a 10–25 % solution in methanol. Before use, the methanol was removed under vacuum and the dendrimers were resuspended in water to a concentration

of 100 μM. H<sub>2</sub>AuCl<sub>4</sub>·3H<sub>2</sub>O (≥ 99.9%), NaBH<sub>4</sub> (99.99%), and the HClO<sub>4</sub> (70% in H<sub>2</sub>O) used for the XAS studies were purchased from Sigma-Aldrich (St. Louis, MO). The HClO<sub>4</sub> used for all other experiments (70% in H<sub>2</sub>O) was purchased from VWR (Radnor, PA). A 1.0 M NaOH solution was purchased from Millipore (Bedford, MA). HPLC grade isopropanol (99.9%) was purchased from Fisher Scientific (Pittsburgh, PA). N<sub>2</sub> (99.9999%), He (99.999%), and O<sub>2</sub> (99.5%) were purchased from Praxair.

Vulcan carbon (EC-72R) was purchased from ElectroChem, Inc. (Woburn, MA). Deionized Millipore water (0.5 MΩ-cm; Millipore, Bedford MA) was used for the XAS studies. Deionized Milli-Q water (DI water, 18.2 MΩ-cm) was used for all other experiments.

### DEN Synthesis

The synthesis of G6-NH<sub>2</sub>(Au<sub>147</sub>) DENs was carried out according to previously published literature reports.<sup>[25,54,56]</sup> Briefly, 147 equiv. of 20 mM H<sub>2</sub>AuCl<sub>4</sub> were added dropwise to a stirred solution of 10.0 μM PAMAM dendrimer. After 2 min, a 10-fold excess of BH<sub>4</sub><sup>-</sup>, dissolved in a 0.30 M NaOH solution, was added. The mixture was then stirred at 22 ± 2 °C for ~12 h to deactivate excess BH<sub>4</sub><sup>-</sup>. This method resulted in a final G6-NH<sub>2</sub>(Au<sub>147</sub>) concentration of 10.0 μM. The same method was used to prepare G6-NH<sub>2</sub>(Au<sub>55</sub>) DENs, except 55 equiv. of H<sub>2</sub>AuCl<sub>4</sub> were used. Following synthesis, the DEN solutions were dialyzed against DI water for 10–15 h using 12 kDa MWCO dialysis tubing (Sigma-Aldrich, St. Louis, MO).<sup>[56]</sup>

Note that the indicated stoichiometries of the DENs (e.g., G6-NH<sub>2</sub>(Au<sub>147</sub>)) reflect the H<sub>2</sub>AuCl<sub>4</sub>:G6-NH<sub>2</sub> ratio used for their synthesis, and therefore they should not be taken as reflecting precise structure. We have, however, shown previously that this ratio controls the average size of DENs.<sup>[50–52]</sup>

### Electrode Preparation

Except for the glassy carbon rod counter electrode, which was from Alfa Aesar (Tewksbury, MA), and the rotating ring-disk electrode (RRDE), which was from Pine Research (Durham, NC), all electrodes were obtained from CH Instruments (Austin, TX). Prior to performing electrochemical measurements, the glassy carbon electrodes (GCEs) were sequentially polished using 1, 0.3, and 0.05 μm alumina. Conductive inks were prepared by, first, sonicating 200 μL of isopropanol with 1.0 mg of Vulcan carbon for 10–15 min. Next, 1.0 mL of a 10.0 μM DEN solution was added to the slurry and sonicated for an additional 10–15 min to ensure adequate dispersion. For electrochemical cleaning experiments, catalyst-coated electrodes were prepared by drop-casting 6.0 μL of this ink onto a 3.0 mm GCE and then drying under a gentle N<sub>2</sub> flow. For electrocatalytic rotating disk voltammograms (RDVs) or rotating ring-disk voltammograms (RRDVs), 16.0 μL of ink were drop-cast onto a 6.0 mm GCE surrounded by a Pt ring and then dried under a gentle N<sub>2</sub> flow.

The foregoing procedure was modified for XAS experiments. After preparing a conductive ink with a 10.0 μM DEN solution, the ink was vacuum filtered through PTFE membrane filters having a 0.5 μm pore size (Advantec MFS Inc., Dublin, CA). The resulting slurry was then immobilized onto Toray Teflon-treated carbon paper (TGP-H-120, The Fuel Cell Store, College Station, TX). For these samples, the Au mass loading was kept consistent at ~30%.

### Electrochemical Measurements

Electrochemical measurements were made using a CH Instruments Model CHI700D Electrochemical Analyzer (Austin, TX). For RDV and

RRDV experiments, the working electrode was rotated using an AFASR2 Rotator from Pine Research (Durham, NC). Electrochemical cleaning studies were carried out in  $N_2$ -saturated, 0.10 M  $HClO_4$ , and electrocatalytic experiments were performed in either  $N_2$ - or  $O_2$ -saturated 0.10 M  $HClO_4$ . The reference electrode,  $Hg/Hg_2SO_4$ , was purchased from CH Instruments (Austin, TX). The counter electrode was a glassy carbon rod purchased from Alfa Aesar (Tewksbury, MA). Each electrochemical cleaning experiment was performed in  $\sim 10$  mL of solution. RDV and RRDV experiments were performed in  $\sim 50$  mL of solution. The measured resistance of the electrolyte solution for the electrochemical experiments was  $\sim 5 \Omega$ .

### Transmission Electron Microscopy (TEM)

Lacey carbon-coated 400 mesh Cu TEM grids were purchased from Electron Microscopy Sciences (Hatfield, PA). Size analysis of AuNPs before and after electrochemical analysis was carried out using a JEOL 2010F TEM having a point-to-point resolution of 0.19 nm and an operating voltage of 200 kV.

Several types of TEM samples were examined. For the as-prepared catalyst ink, 0.5  $\mu L$  of DENs solution was diluted with 2.0  $\mu L$  of DI water, and the resulting solution drop-cast onto a lacey carbon-coated Cu TEM grid. Following electrochemical analysis and rinsing with DI water, the TEM sample was obtained by gently wiping a lacey carbon-coated Cu grid across the wetted surface of the GCE. Size distributions were determined by using ImageJ to analyze 200 NPs from each of three independent electrochemical experiments, followed by fitting of the data using the Gaussian function within the OriginLab software package (Northampton, MA). The size distributions were weighted by NP volume as discussed in Section S1 of the SI.

### X-ray Absorption Spectroscopy (XAS)

XAS measurements, including X-ray absorption near edge structure (XANES) and extended X-ray absorption fine structure (EXAFS), were performed at the Au  $L_3$ -edge in fluorescence mode at the 7-BM QAS beamline at the National Synchrotron Light Source II (NSLS-II) at Brookhaven National Laboratory. The Au foil reference spectrum was collected concurrently with the samples. This reference spectrum is used for X-ray energy calibration, spectral alignment, and determination of the amplitude reduction factor for fitting.

*In situ* electrochemical measurements were carried out using a Bio-Logic Science Instruments Model VSP-300 multichannel potentiostat (Knoxville, TN). Electrochemical cleaning experiments were carried out in He-purged 0.10 M  $HClO_4$ , with a constant gas flow over the surface of the solution during measurements. The electrodes consisted of a Toray Teflon-treated carbon paper working electrode (described earlier), a Pt counter electrode, and a leakless Ag/AgCl reference electrode (eDAQ, Colorado Springs, CO). All potentials were converted to the  $Hg/Hg_2SO_4$  reference scale for ease of comparison to other data presented in this article. The first XAS spectrum was obtained before electrochemical cleaning with the working electrode potential held at  $-200$  mV vs.  $Hg/Hg_2SO_4$  for  $\sim 5$  min. Subsequent spectra were obtained by repeating this process, but after three potential excursions to increasingly positive limits.

XAS data were processed and analyzed using the Athena and Artemis software within the IFEFFIT package. The least-squares fitting of EXAFS data was performed for both  $G6-NH_2(Au_{147})$  and  $G6-NH_2(Au_{55})$  DENs. The amplitude reduction factor ( $S_0^2$ ) was obtained by fitting the Au foil spectrum, and then this value was fixed for the subsequent fitting of the DEN spectra. The first nearest

neighbor Au–Au photoelectron path was calculated with the FEFF6.2 program, using the fcc crystal structure coordinates of Au, and was subsequently included in the fits of all DENs data. The Au–Cl photoelectron path, calculated using a  $AuCl_3$  structure, was included in the data fitting to improve the fitting quality. In all fits, the energy shifts ( $\Delta E_0$ ) of the Au–Au and Au–Cl paths were constrained to be the same for each DEN size at each potential limit. The EXAFS data for  $G6-NH_2(Au_{147})$  and  $G6-NH_2(Au_{55})$  DENs at 900 mV were fitted simultaneously by constraining the energy shifts and disorder parameters of the Au–Au pairs to the same values, which helped to break the correlation between fitting parameters. Such a constraint was justified based on the size information obtained from TEM measurements. From the fitting results, the coordination numbers ( $N$ ), bond lengths ( $R$ ), and associated Debye-Waller factors ( $\sigma^2$ ) were extracted for each DEN size at each potential limit.

## 2. Results and Discussion

### 2.1. Preparation and Characterization of $G6-NH_2(Au_{147})$ and $G6-NH_2(Au_{55})$ Conductive Inks

As discussed in the Experimental Section, PAMAM dendrimers were used as templates to prepare  $G6-NH_2(Au_n)$  DENs, ( $n = 147$  or 55). Vulcan carbon was used to prepare the conductive inks. TEM analysis indicated that the size of the  $G6-NH_2(Au_{147})$  and  $G6-NH_2(Au_{55})$  DENs in the ink were  $1.8 \pm 0.2$  and  $1.4 \pm 0.2$  nm, respectively (Figure S1). These sizes are consistent with those in previous reports.<sup>[51]</sup>

### 2.2. Electrochemical Cleaning Experiments

As discussed in the Introduction, electrocatalytic NPs are often subjected to a potential cycling protocol to remove impurities from their surfaces and to determine their electrochemically active surface areas (ECSA). Here, for example, we carried out what will be subsequently referred to as ‘cleaning scans’ by cycling the working electrode potential three times from a starting potential of  $-200$  mV, to progressively more positive potentials (100, 300, 500, 700, and 900 mV), and then to  $-650$  mV. Representative cyclic voltammograms (CVs) for the first scans are shown in Figure 1. The CVs were scanned at 50 mV/s in aqueous,  $N_2$ -saturated 0.10 M  $HClO_4$ . These same parameters were used for the companion XAS and TEM measurements discussed later.

For scans to 100 mV and 300 mV, only capacitive current is observed for both the  $G6-NH_2(Au_{147})$  DENs, Figure 1a, and  $G6-NH_2(Au_{55})$  DENs, Figure 1b. Expanded views of these voltammograms are provided in Figure S2. A slight anodic faradaic current is observed for both DEN sizes at 500 mV (Figure S2). The faradaic current becomes more pronounced at 700 mV, where the onset of a reduction peak is also just visible in both frames of Figure 1. Finally, at 900 mV, both Au oxidation and reduction peaks are well developed. The anodic current arises from oxidation of the AuNP surface, which may lead to formation of either  $AuO_x$  or  $Au^+$  in the case of smaller NPs.<sup>[7,8,57,58]</sup> When the potential is reversed, the reduction feature at  $\sim 340$  mV

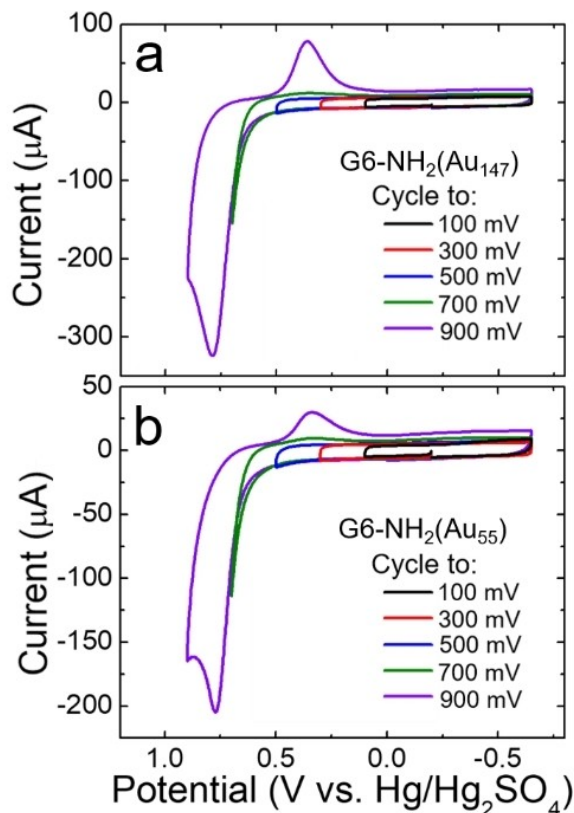


**Figure 1.** Cleaning CVs for (a) G6-NH<sub>2</sub>(Au<sub>147</sub>) and (b) G6-NH<sub>2</sub>(Au<sub>55</sub>) DENs obtained in N<sub>2</sub>-saturated, 0.10 M HClO<sub>4</sub>. The potential was scanned three times at 50 mV/s from –200 mV to the positive potential limits indicated in the legend before being cycled back to –650 mV. A representative CV from the first scan is shown.

corresponds to reduction of oxidized Au products. This latter point will be discussed in more detail later.<sup>[4,59]</sup>

The changes in the areas under the Au reduction peaks at ~340 mV, over the course of three potential cycles to 900 mV, were calculated to determine the stability of the Au DENs (Figure S3). Between the first and second cycles for both the G6-NH<sub>2</sub>(Au<sub>147</sub>) and G6-NH<sub>2</sub>(Au<sub>55</sub>) DENs, the areas under the peaks increased by 8 ± 3%. Between the second and third cycles, the areas increased by only 2 ± 1% for both sizes of DENs. This smaller increase in the peak areas is consistent with increases observed in similar studies and may be attributable to removal of impurities from the AuNP surfaces.<sup>[4,24]</sup>

The key finding from this part of the study is that the cleaning scans for both G6-NH<sub>2</sub>(Au<sub>147</sub>) and G6-NH<sub>2</sub>(Au<sub>55</sub>) are quite similar. This is somewhat surprising, because previous reports have shown that 1.4 nm AuNPs should oxidize ~130 mV before 1.8 nm AuNPs.<sup>[60,61]</sup> As we will discuss later, it is likely that even potential excursions to 100 mV already result in growth of the 1.4-nm G6-NH<sub>2</sub>(Au<sub>55</sub>) DENs. This means that at potentials positive of 100 mV, a substantial fraction of G6-NH<sub>2</sub>(Au<sub>55</sub>) may already be indistinguishable from G6-NH<sub>2</sub>(Au<sub>147</sub>), thereby accounting for the similarity of the CVs in Figure 1.

### 2.3. Transmission Electron Microscopy (TEM)

To better understand the results discussed in the previous section, *ex-situ* TEM was performed following each CV experiment. The size-distribution histograms obtained via TEM were weighted by volume (Section S1 in the SI) to facilitate comparison to the XAS measurements discussed later.

First, consider the case of the G6-NH<sub>2</sub>(Au<sub>147</sub>) DENs. Figure 2 provides typical TEM micrographs (at two different magnifications) and size-distribution histograms for these materials before (top row) and after (bottom rows) cleaning in the same potential ranges and under the same conditions used to obtain the data shown in Figure 1a. The average NP sizes obtained from fitting the volume-weighted size-distribution histograms show that the average sizes of G6-NH<sub>2</sub>(Au<sub>147</sub>) DENs change just

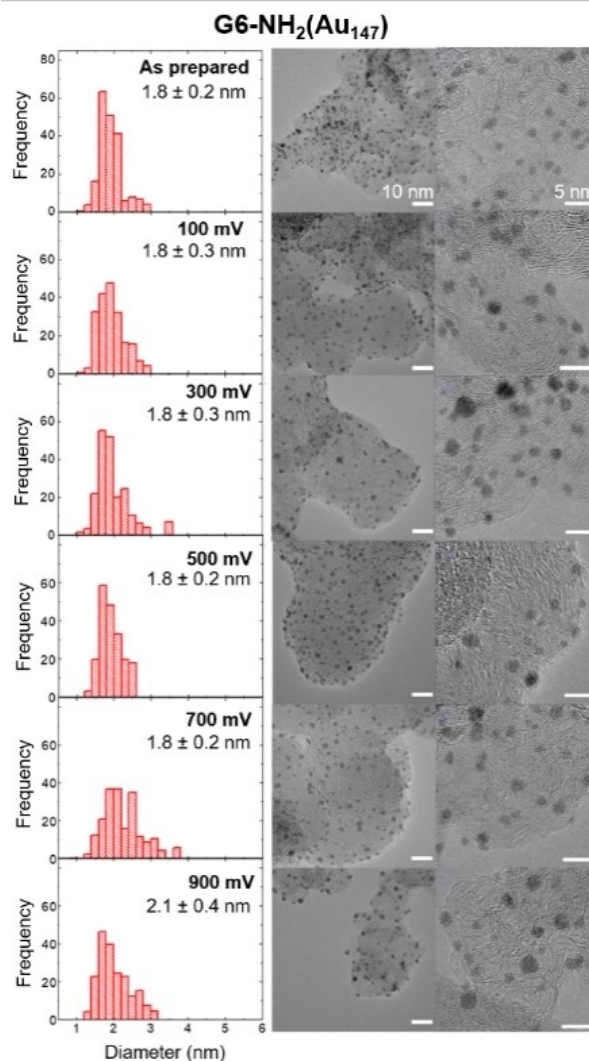


**Figure 2.** TEM micrographs (at two different magnifications) and size-distribution histograms for G6-NH<sub>2</sub>(Au<sub>147</sub>) DENs before (top row) and after (bottom rows) electrochemical cleaning scans to the positive potentials shown in the legends. Cleaning was carried out in the same potential ranges and under the same conditions used to obtain the data shown in Figure 1a. The size-distribution histograms were constructed by measuring the diameter of 200 NPs and weighting by volume.

slightly with increasing positive potential scan limit. Specifically, the average volume-weighted NP diameter is 1.8 nm until the scan limit reaches 900 mV, at which point it increases to  $2.1 \pm 0.4$  nm.

Although the average volume-weighted diameter of the G6-NH<sub>2</sub>(Au<sub>147</sub>) DENs does not change until a potential of 900 mV is reached, differences in the shapes of the histograms provide insight into the effect of potential on the NPs. Specifically, Figure 2 shows that as the limiting potential increases, more large NPs and fewer small NPs are generally present, as indicated by skewing of the distribution toward the right side of the histograms. This observation is consistent with an Ostwald ripening growth mechanism wherein unstable smaller NPs dissolve and redeposit on the surface of larger NPs.<sup>[62,63]</sup> This mechanistic point will be discussed in more detail later.

In contrast to the G6-NH<sub>2</sub>(Au<sub>147</sub>) DENs, the G6-NH<sub>2</sub>(Au<sub>55</sub>) DENs grow in size even with excursions to modest positive potentials (Figure 3). For example, after scanning the potential of the G6-NH<sub>2</sub>(Au<sub>55</sub>) DENs three times from  $-200$  mV to 300 mV (Figure 1b), the average NP size increased from  $1.4 \pm 0.2$  nm (as prepared) to  $1.7 \pm 0.3$  nm. Interestingly, this size change occurs despite the observation that no detectable faradaic current flows in this potential range (Figure S2b). After scanning to 700 mV, which leads to the onset of a clear faradaic oxidation current in the corresponding CV (Figure 1b), the diameter increases further to  $1.8 \pm 0.4$  nm. Finally, following cleaning to 900 mV, the average DEN size increases to  $2.2 \pm 0.5$  nm, which is about the same as for the G6-NH<sub>2</sub>(Au<sub>147</sub>) DENs ( $2.1 \pm 0.4$  nm). The size distribution for the G6-NH<sub>2</sub>(Au<sub>55</sub>) DENs generally skews towards the right side of the histograms as the limiting potential increases, just as it did for the G6-NH<sub>2</sub>(Au<sub>147</sub>) DENs.

The progressive NP growth observed via TEM is significant for two reasons. First, these increases are observed after just three cleaning scans to each potential. This is in contrast to other studies showing that such changes occur after hundreds to thousands of cycles.<sup>[7,8,24]</sup> Second, size changes are observed for G6-NH<sub>2</sub>(Au<sub>55</sub>) DENs even before faradaic oxidation or reduction currents are detected in the CVs. Both of these observations suggest that the size of the G6-NH<sub>2</sub>(Au<sub>55</sub>) DENs is particularly sensitive to even modest potential excursions.

#### 2.4. X-ray Absorption Spectroscopy (XAS)

To better understand the CVs and size changes discussed in the previous sections, *in-situ* XAS measurements of Au DENs were obtained following electrochemical cleaning scans. For these studies, the electrode was cycled three times between the same potential limits used for the CVs and TEM analysis, and then the potential was held at  $-200$  mV for the duration of the XAS measurements. The latter potential was selected to prevent further electrochemical oxidation or NP growth during the XAS scans. The CVs obtained just prior to XAS measurements (Figure S4) were consistent with the cleaning CVs shown in Figure 1. Additionally, XANES spectra collected at the Au L<sub>3</sub>-edge for both sizes of DENs have absorption edge energies and features similar to that of the Au foil, indicating that the NPs

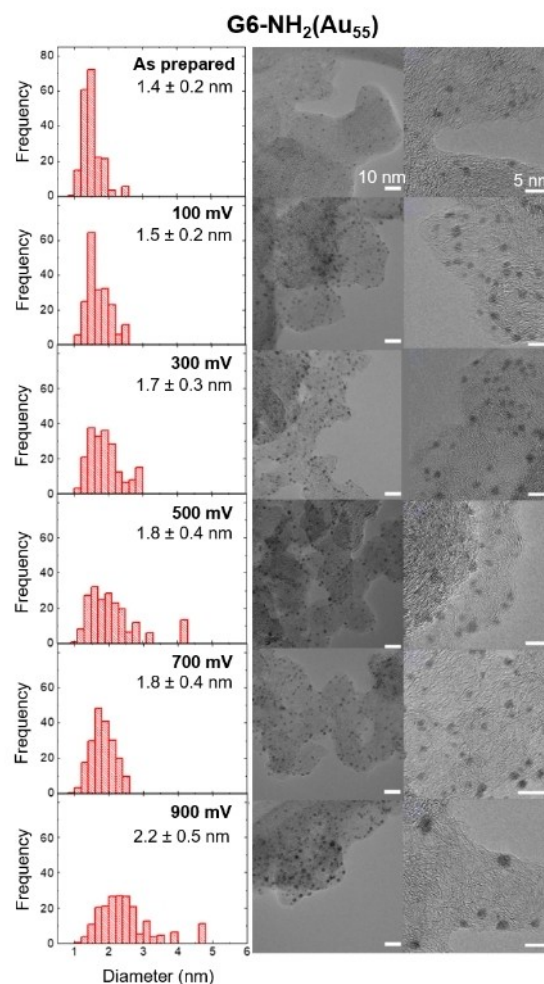


**Figure 3.** TEM micrographs (at two different magnifications) and size-distribution histograms for G6-NH<sub>2</sub>(Au<sub>55</sub>) DENs before (top row) and after (bottom rows) electrochemical cleaning scans to the positive potentials shown in the legends. Cleaning was carried out in the same potential ranges and under the same conditions used to obtain the data shown in Figure 1b. The size-distribution histograms were constructed by measuring the diameter of 200 NPs and weighting by volume.

were mainly metallic before and after the cleaning scans (Figure S5).

Local NP structural information can be obtained from the Fourier transformed magnitudes of the  $k^2$ -weighted EXAFS spectra at the Au L<sub>3</sub>-edge (also known as the  $R$ -space spectra). The  $k^2$ -weighted EXAFS spectra used to construct the Fourier transforms are provided in Figure S6. In spectra such as these, an increase in particle size is signaled by an increase in the intensity of the peaks (which corresponds to the higher average atomic coordination number that is found in larger NPs).<sup>[64]</sup> Indeed, qualitative examination of the  $R$ -space features for the DEN spectra (Figure 4) indicates an increase in the peak height, and hence NP growth, as the positive scan limit increases.

To obtain quantitative structural information as a function of the positive potential scan limit, EXAFS fitting was performed as described in the Experimental Section. Key results extracted from the EXAFS data are provided in Table 1 and complete

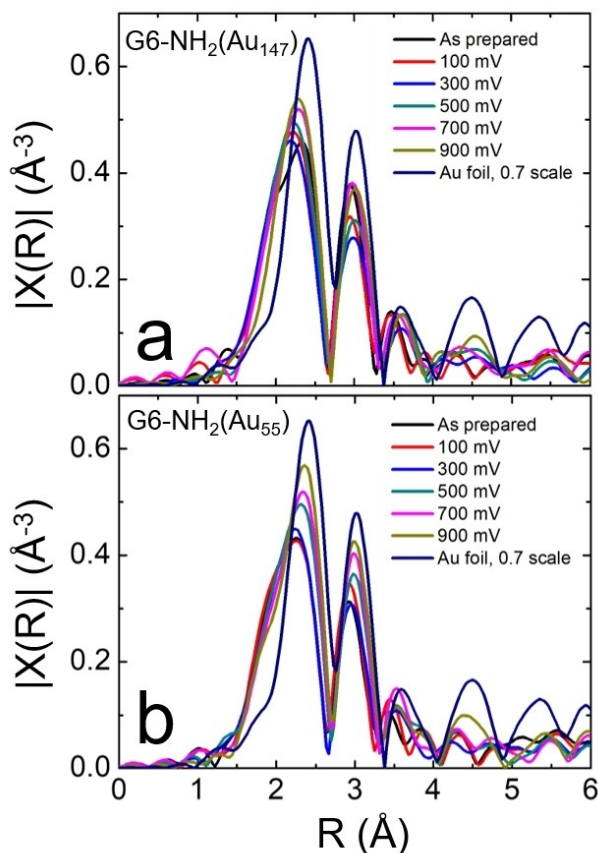


**Figure 4.** Fourier transformed magnitudes of the  $k^2$ -weighted EXAFS spectra (also known as the  $R$ -space spectra) at the Au  $L_3$ -edge for (a) G6-NH<sub>2</sub>(Au<sub>147</sub>) DENs and (b) G6-NH<sub>2</sub>(Au<sub>55</sub>) DENs ( $k$ -range: 2–10 Å<sup>-1</sup>;  $R_{\text{bkg}} = 1.2$  Å). The  $k^2$ -weighted EXAFS spectra used to construct the Fourier transformed spectra are provided in Figure S6. Prior to the XAS measurements, the electrode was cycled three times in He-saturated, 0.10 M HClO<sub>4</sub> to the potential limits indicated in the legends. The electrode potential was then held at –200 mV for the duration of the XAS measurements. The Au foil standard spectra were multiplied by a constant value of 0.70 for better visual comparison with the Au DENs spectra.

fitting results, including the  $k$ - and  $R$ -ranges used to process and fit the data, are provided in Tables S1 and S2. The

magnitudes of the EXAFS spectra and fits in  $R$ -space for both G6-NH<sub>2</sub>(Au<sub>147</sub>) and G6-NH<sub>2</sub>(Au<sub>55</sub>) DENs, at each potential limit, are provided in Figure S7. NP diameters determined by EXAFS were calculated using the average coordination number,  $N_{(\text{Au}-\text{Au})}$ , to facilitate comparison to the TEM results discussed earlier. The procedure for calculating particle diameter from  $N_{(\text{Au}-\text{Au})}$  is provided in Section S2 of the SI.<sup>[51,65,66]</sup> This calculation is modeled using a quasispherical NP shape, which approximates the shape of the DENs.

Unlike TEM, in which the diameter of each NP is measured independently,  $N_{(\text{Au}-\text{Au})}$  represents an average value for all NPs in the sample. Moreover, EXAFS is a volumetric technique, and therefore larger NPs contribute disproportionately to  $N_{(\text{Au}-\text{Au})}$ . Accordingly, direct comparison of NP sizes determined by TEM and EXAFS requires weighting the TEM size distributions by NP volume.<sup>[67,68]</sup> For monodisperse NPs, weighting by volume will not have a significant effect on the size distribution. For more polydisperse samples, however, especially those containing a significant fraction of larger NPs, weighting by volume can significantly alter the size-distribution histogram.<sup>[68,69]</sup>

For G6-NH<sub>2</sub>(Au<sub>147</sub>),  $N_{(\text{Au}-\text{Au})}$  for the as-prepared DENs is  $8.8 \pm 2.2$ , which corresponds to a diameter of  $1.8 \pm 0.5$  nm and is therefore in accord with the volume-weighted TEM diameter of  $1.8 \pm 0.2$  nm (Table 1). As the G6-NH<sub>2</sub>(Au<sub>147</sub>) DENs are cleaned to increasingly positive potentials, a general increase in  $N_{(\text{Au}-\text{Au})}$  is observed (Table 1). After scanning to 900 mV,  $N_{(\text{Au}-\text{Au})}$  increases to  $9.9 \pm 0.7$ , which corresponds to a diameter of  $2.9 \pm 0.3$  nm. This calculated diameter compares to the volume-weighted TEM measurement of  $2.1 \pm 0.4$  nm.

While the diameters of the G6-NH<sub>2</sub>(Au<sub>147</sub>) DENs calculated from the EXAFS measurements generally increase as a result of electrochemical cleaning, the average volume-weighted diameters obtained from TEM measurements remain constant until the DENs are cleaned to 900 mV (Figure 2). As mentioned earlier, however, the evolution of the TEM size distributions suggest that larger NPs form during electrochemical cleaning scans. These larger NPs do not significantly change the average diameter determined by TEM, but they do disproportionately contribute to  $N_{(\text{Au}-\text{Au})}$ .<sup>[68,69]</sup> Accordingly, the increases in  $N_{(\text{Au}-\text{Au})}$  upon cleaning reflect the changes in the shape of the volume-weighted TEM size-distribution histograms (Figure 2).

**Table 1.** Results extracted from the TEM and EXAFS data for G6-NH<sub>2</sub>(Au<sub>147</sub>) and G6-NH<sub>2</sub>(Au<sub>55</sub>) DENs. Complete fitting data for EXAFS, including the  $k$ - and  $R$ -ranges for data processing and analysis, are provided in Tables S1 and S2. The magnitudes of the EXAFS spectra in  $R$ -space and their corresponding fits are shown in Figure S7.  $N_{(\text{Au}-\text{Au})}$  refers to the average Au–Au coordination number and  $R_{(\text{Au}-\text{Au})}$  to the Au–Au bond length. EXAFS diameters were calculated using  $N_{(\text{Au}-\text{Au})}$  (Section S2 in the SI).<sup>[51,65]</sup> The error bars in the EXAFS diameter were calculated by propagating the uncertainties of the EXAFS measurements. The TEM diameters were determined from TEM micrographs and then volume-weighted to facilitate direct comparison to the EXAFS diameter (Section S1 in the SI). The error bars in the volume-weighted TEM diameter are the standard deviations of the particle size distributions.

Potential (mV)	G6-NH <sub>2</sub> (Au <sub>147</sub> )				G6-NH <sub>2</sub> (Au <sub>55</sub> )			
	$N_{(\text{Au}-\text{Au})}$	EXAFS Diameter [nm]	Volume-Weighted TEM Diameter [nm]	$R_{(\text{Au}-\text{Au})}$ [Å]	$N_{(\text{Au}-\text{Au})}$	EXAFS Diameter [nm]	Volume-Weighted TEM Diameter [nm]	$R_{(\text{Au}-\text{Au})}$ [Å]
As prepared	$8.8 \pm 2.2$	$1.8 \pm 0.5$	$1.8 \pm 0.2$	$2.81 \pm 0.01$	$7.9 \pm 0.7$	$1.3 \pm 0.3$	$1.4 \pm 0.2$	$2.79 \pm 0.01$
100	$9.0 \pm 1.6$	$1.9 \pm 0.4$	$1.8 \pm 0.3$	$2.81 \pm 0.01$	$7.9 \pm 0.9$	$1.3 \pm 0.3$	$1.5 \pm 0.2$	$2.78 \pm 0.01$
300	$9.0 \pm 1.0$	$1.9 \pm 0.3$	$1.8 \pm 0.3$	$2.81 \pm 0.01$	$8.7 \pm 0.8$	$1.7 \pm 0.3$	$1.7 \pm 0.3$	$2.80 \pm 0.01$
500	$10.0 \pm 1.2$	$3.0 \pm 0.4$	$1.8 \pm 0.2$	$2.82 \pm 0.01$	$9.7 \pm 1.1$	$2.6 \pm 0.4$	$1.8 \pm 0.4$	$2.82 \pm 0.01$
700	$9.9 \pm 1.3$	$2.9 \pm 0.4$	$1.8 \pm 0.2$	$2.82 \pm 0.01$	$9.7 \pm 1.2$	$2.6 \pm 0.4$	$1.8 \pm 0.4$	$2.83 \pm 0.01$
900	$9.9 \pm 0.7$	$2.9 \pm 0.3$	$2.1 \pm 0.4$	$2.830 \pm 0.004$	$10.0 \pm 0.6$	$3.0 \pm 0.3$	$2.2 \pm 0.5$	$2.835 \pm 0.003$

For G6-NH<sub>2</sub>(Au<sub>55</sub>) DENs,  $N_{(\text{Au-Au})}$  is  $7.9 \pm 0.7$  before cleaning, which corresponds to a calculated diameter of  $1.3 \pm 0.3$  nm. This is close to the volume-weighted diameter of  $1.4 \pm 0.2$  nm determined from the TEM data. As with the G6-NH<sub>2</sub>(Au<sub>147</sub>) DENs, analysis of  $N_{(\text{Au-Au})}$  for G6-NH<sub>2</sub>(Au<sub>55</sub>) DENs following cleaning scans reveals a nearly monotonic increase, which is consistent with the volume-weighted TEM diameters shown in Table 1. For example, at the 900 mV potential limit,  $N_{(\text{Au-Au})}$  is  $10.0 \pm 0.6$ , which corresponds to a calculated diameter of  $3.0 \pm 0.3$  nm. This is approximately the same size as the G6-NH<sub>2</sub>(Au<sub>147</sub>) DENs after cleaning to 900 mV, and it also compares to the corresponding volume-weighted TEM diameter of the G6-NH<sub>2</sub>(Au<sub>55</sub>) DENs ( $2.2 \pm 0.5$  nm).

The interatomic bond distance,  $R_{(\text{Au-Au})}$ , can also be extracted from the EXAFS data. The value of  $R_{(\text{Au-Au})}$  for the as-prepared G6-NH<sub>2</sub>(Au<sub>147</sub>) DENs is  $2.81 \pm 0.01$  Å, which increases by only  $0.02$  Å to  $2.830 \pm 0.004$  Å following cleaning scans (Table 1). In contrast,  $R_{(\text{Au-Au})}$  for the as-prepared G6-NH<sub>2</sub>(Au<sub>55</sub>) DENs is  $2.79 \pm 0.01$  Å, which increases nearly monotonically as the DENs are cycled to increasingly positive potentials (Table 1). For example,  $R_{(\text{Au-Au})}$  increases by  $0.045$  Å, to  $2.835 \pm 0.003$  Å, after cleaning to 900 mV. This increase is more than double that observed for the G6-NH<sub>2</sub>(Au<sub>147</sub>) DENs, suggesting that more NP growth and structural changes occur for the G6-NH<sub>2</sub>(Au<sub>55</sub>) DENs.<sup>[70–72]</sup> This finding is consistent with the TEM results, which indicate that the smaller G6-NH<sub>2</sub>(Au<sub>55</sub>) DENs undergo more substantial size changes upon cleaning than the larger G6-NH<sub>2</sub>(Au<sub>147</sub>) DENs.

## 2.5. Effect of DEN Size Changes on the Kinetics of the Electrocatalytic ORR

We now turn our attention to how the changes in NP size and structure described in the previous sections affect the electrocatalytic function of DENs.<sup>[25,38,39,73]</sup>

As discussed in the Experimental Section, the RRDE used for the electrocatalysis experiments consisted of a glassy carbon disk and a Pt ring. Prior to electrocatalysis, the potential of the DEN-modified RRDE was cycled three times in N<sub>2</sub>-saturated, 0.10 M HClO<sub>4</sub> using the same parameters and potential limits used for the CVs shown in Figure 1. For these cleaning scans, the RRDE was not rotated. Next, a set of background RRDVs (with rotation) were collected in N<sub>2</sub>-saturated, 0.10 M HClO<sub>4</sub>. Finally, electrocatalytic data were collected in O<sub>2</sub>-saturated, 0.10 M HClO<sub>4</sub>.

The aforementioned background RRDVs are provided in Figure S8, which shows scans for both the disk and ring electrodes. For the background RRDVs, the potential of the disk was swept from 0 to  $-800$  mV, the potential of the ring electrode was held at 500 mV, and the electrode was rotated at rates between 400 and 1600 rpm. The background RRDVs were subsequently subtracted from the electrocatalytic RRDVs and RRDVs discussed next.

Figure 5a shows representative ORR RDVs (1600 rpm) obtained before (as prepared) and after performing cleaning scans to 900 mV on the DEN-modified electrodes in N<sub>2</sub>-saturated 0.10 M HClO<sub>4</sub>. The current densities in these RDVs

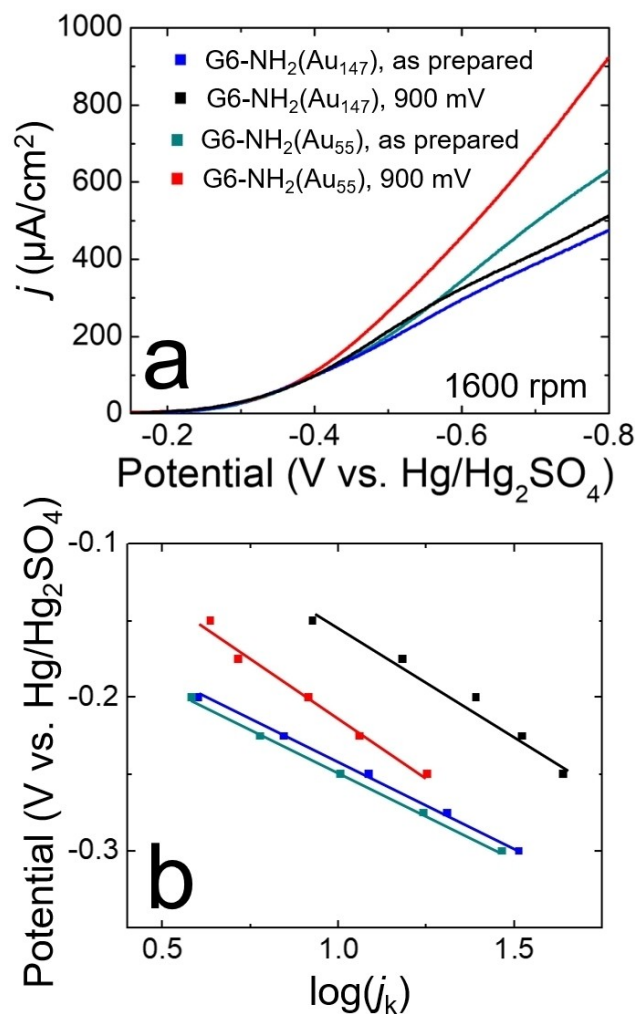


**Figure 5.** (a) RDVs of G6-NH<sub>2</sub>(Au<sub>147</sub>) and G6-NH<sub>2</sub>(Au<sub>55</sub>) DENs in O<sub>2</sub>-saturated, 0.10 M HClO<sub>4</sub>. Before electrocatalysis, the DENs were cleaned to 900 mV using the same conditions as in Figure 1. For electrocatalytic measurements, the potential was scanned at 5 mV/s between 0 and  $-800$  mV while rotating the electrode at 1600 rpm. (b) Tafel plots for Au DENs before and after cleaning to 900 mV. The linear range used to calculate the Tafel slopes was determined to be between  $-200$  and  $-300$  mV for as-prepared DENs and between  $-150$  and  $-250$  mV for DENs after cleaning to 900 mV.

were normalized to the Au ECSA by integrating the current under the AuO<sub>x</sub> reduction peak, present at  $\sim 340$  mV, in the last of the three cleaning scans to 900 mV (Figure S3). A positive potential of  $\sim 900$  mV is typically used for AuNP cleaning scans and surface area determination.<sup>[24,25,40,73–75]</sup> The generally accepted factor of  $390 \mu\text{C}/\text{cm}^2$  was used for this calculation.<sup>[59,74,76]</sup>

The RDV for the as-prepared G6-NH<sub>2</sub>(Au<sub>147</sub>) DENs (Figure 5a, blue) and the RDV obtained after cleaning to 900 mV (black) are similar. In contrast to the data for the G6-NH<sub>2</sub>(Au<sub>147</sub>) DENs, a significant increase in current density, related to enhanced electrocatalytic activity, is observed after scanning the G6-NH<sub>2</sub>(Au<sub>55</sub>) DENs to 900 mV (red). Considering the TEM and XAS results discussed earlier, this improvement in electrocatalytic performance is likely due to a cleaning-induced increase in NP size.

To quantify changes in electrocatalytic ORR activity following electrochemical cleaning scans, ECSA-normalized current density values were extracted from the RDVs at  $-350$  mV. The current density for as-prepared G6-NH<sub>2</sub>(Au<sub>147</sub>) DENs was  $53 \pm 9$   $\mu\text{A}/\text{cm}^2$ , which increased to  $73 \pm 5$   $\mu\text{A}/\text{cm}^2$  after cleaning to 900 mV. For the G6-NH<sub>2</sub>(Au<sub>55</sub>) DENs, the initial current density was  $40 \pm 9$   $\mu\text{A}/\text{cm}^2$ , which increased to  $68 \pm 9$   $\mu\text{A}/\text{cm}^2$  after cleaning scans to 900 mV. The observed increase in current density after cycling to 900 mV may suggest that cleaning-induced NP growth results in increased catalytic activity, and that G6-NH<sub>2</sub>(Au<sub>55</sub>) DENs are particularly sensitive to the effects of cleaning scans.<sup>[75]</sup>

An additional control experiment was performed to determine if ORR electrocatalysis itself (e.g., in the absence of cleaning scans) causes the as-prepared G6-NH<sub>2</sub>(Au<sub>55</sub>) DENs to grow in size. The results show that if the electrode is not cleaned in N<sub>2</sub>-saturated, 0.10 M HClO<sub>4</sub> prior to electrocatalysis, then the average volume-weighted diameter of the G6-NH<sub>2</sub>(Au<sub>55</sub>) DENs does not change significantly (Figure S9). We conclude that the ORR itself does not induce NP growth for G6-NH<sub>2</sub>(Au<sub>55</sub>) DENs. That is, only the cleaning scans to positive potentials result in NP growth.

There are two significant outcomes from the electrocatalysis experiments discussed thus far. First, reproducible and significant changes arise in ORR voltammograms obtained after performing electrochemical cleaning scans to 900 mV for G6-NH<sub>2</sub>(Au<sub>55</sub>) DENs. This, along with an increase in current density at  $-350$  mV for both DENs, suggests changing electrocatalytic activity consistent with the observed NP growth. Second, due to slow electron-transfer kinetics and the high overpotentials required for the ORR at AuNPs in acid, a limiting current is not observed for these RDVs.<sup>[40,73]</sup> This latter point will be discussed in more detail next.

Using RDVs obtained in O<sub>2</sub>-saturated, 0.10 M HClO<sub>4</sub> at rotation rates ranging between 400 and 1600 rpm (Figure S10), Koutecký-Levich (K-L) plots were constructed by extracting current density values from the disk electrode for both G6-NH<sub>2</sub>(Au<sub>147</sub>) and G6-NH<sub>2</sub>(Au<sub>55</sub>) DENs at a range of potentials. Previous reports have shown that meaningful results can be obtained using this approach, even in the absence of well-defined limiting currents.<sup>[2,40,73]</sup> Representative K-L plots for G6-NH<sub>2</sub>(Au<sub>147</sub>) and G6-NH<sub>2</sub>(Au<sub>55</sub>) DENs (both as-prepared and after cleaning scans to 900 mV) extracted at potentials ranging from  $-300$  to  $-600$  mV are shown in Figure S11. K-L analysis predicts a linear relationship between the inverse current density ( $j^{-1}$ ) and the inverse square root of rotation rate ( $\omega^{-1/2}$ ) and indeed this relationship is observed in the experimental results.<sup>[38,77]</sup>

The K-L plots can be used to construct Tafel plots for the DEN electrocatalysts. A Tafel analysis provides kinetic information about the rate-determining step in a multi-step electron transfer mechanism.<sup>[78]</sup> This is particularly important for these experiments because of the absence of a well-defined limiting current in the RDVs (Figure S10). As shown in Figure 5b, the linear range of the Tafel plots for the as-prepared DENs is between  $-200$  mV and  $-300$  mV, while the linear Tafel range after cleaning to 900 mV is between  $-150$  mV and  $-250$  mV.

The linear ranges of the Tafel plots were selected in accordance with literature methods for Tafel analyses constructed for the ORR using similarly sized AuNPs.<sup>[73,79,80]</sup> The slopes of the linear regions of the Tafel plots can then be analyzed to compare reaction rates for the G6-NH<sub>2</sub>(Au<sub>147</sub>) and G6-NH<sub>2</sub>(Au<sub>55</sub>) DENs before and after cleaning scans.<sup>[73,75,79,80]</sup>

The Tafel slope for the as-prepared G6-NH<sub>2</sub>(Au<sub>147</sub>) DENs (Figure 5b, blue) is 109 mV/decade. This value is consistent with literature values for Tafel slopes measured in acid for similarly sized AuNPs: 111.1 mV/decade<sup>[73]</sup> and 120 mV/decade.<sup>[75]</sup> After carrying out cleaning scans to 900 mV in N<sub>2</sub>-saturated, 0.10 M HClO<sub>4</sub> (black), the Tafel slope increases from 109 mV/decade to 138 mV/decade, indicating a suppression of ORR kinetics.<sup>[79]</sup>

The results of the Tafel analysis for the as-prepared G6-NH<sub>2</sub>(Au<sub>55</sub>) DENs (slope = 112 mV/decade, Figure 5b, green) are similar to that of the G6-NH<sub>2</sub>(Au<sub>147</sub>) DENs (slope = 109 mV/decade). After cleaning scans to 900 mV (red), however, the Tafel slope for the G6-NH<sub>2</sub>(Au<sub>55</sub>) DENs increases to 156 mV/decade (compared to 138 mV/decade for the G6-NH<sub>2</sub>(Au<sub>147</sub>) DENs).

These results reflect a significantly higher percentage suppression of the ORR kinetics for the smaller G6-NH<sub>2</sub>(Au<sub>55</sub>) DENs after the three cleaning scans. That is, the relative change in the Tafel slopes is 39% for the smaller DENs and just 23% for the larger DENs. We conclude, therefore, that the cleaning scan-induced NP growth observed via TEM and EXAFS leads to significant suppression of the ORR kinetics for the DENs. This observation is consistent with literature reports that the catalytic activity of AuNPs is strongly size-dependent.<sup>[25,28,38,39,41,81]</sup>

## 2.6. Effect of DEN Size Changes on the Number of Electrons Transferred during the Electrocatalytic ORR

An RRDE analysis was used to determine  $n_{\text{eff}}$  which is the number of electrons transferred per molecule of O<sub>2</sub> for DENs following the cleaning scans shown in Figure 1. Representative RRDEs for the as-prepared G6-NH<sub>2</sub>(Au<sub>147</sub>) and G6-NH<sub>2</sub>(Au<sub>55</sub>) DENs are available in the Supporting Information (Figure S10).

The RRDE data were analyzed using eq 1.<sup>[82]</sup> Here,  $N$  is the collection efficiency for the RRDE used for electrocatalytic experiments ( $38.5 \pm 0.1$ ),  $i_d$  is current at the disk electrode, and  $i_r$  is current at the ring electrode. For these calculations,  $i_d$  and  $i_r$  were extracted at  $-350$  mV.

$$n_{\text{eff}} = 4 \left( \frac{Ni_d}{Ni_d + i_r} \right) \quad (1)$$

Small but significant changes in  $n_{\text{eff}}$  are observed for both sizes of DENs following cleaning scans in N<sub>2</sub>-saturated, 0.10 M HClO<sub>4</sub> (Figure 6). For the as-prepared G6-NH<sub>2</sub>(Au<sub>147</sub>) DENs (black),  $n_{\text{eff}} = 2.8 \pm 0.1$ , and it increases by only 0.2 after three cleaning scans to 900 mV. For the as-prepared G6-NH<sub>2</sub>(Au<sub>55</sub>) DENs (red), the initial  $n_{\text{eff}}$  value is  $2.5 \pm 0.1$ , which is lower than that of the G6-NH<sub>2</sub>(Au<sub>147</sub>) DENs ( $2.8 \pm 0.1$ ). After three cleaning scans to 900 mV, however, it increases by 0.5, to  $3.0 \pm 0.1$ , which

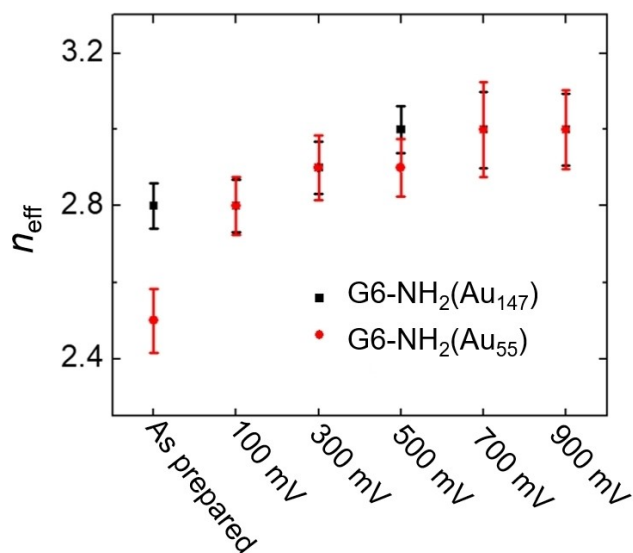


**Figure 6.** Plot showing changes in  $n_{\text{eff}}$  as a function of the positive potential limit for G6-NH<sub>2</sub>(Au<sub>147</sub>) and G6-NH<sub>2</sub>(Au<sub>55</sub>) DENs. Prior to electrocatalytic ORR experiments, cleaning scans were carried out in the same potential ranges and under the same conditions used to obtain the data in Figure 1. Electrocatalytic ORR experiments were carried out in O<sub>2</sub>-saturated, 0.10 M HClO<sub>4</sub>. The disk potential was scanned at 5 mV/s between 0 and -800 mV, the ring potential was held at 500 mV, and the electrode was rotated at 1600 rpm. To calculate  $n_{\text{eff}}$  (eq 1), current values from three independent trials, represented by the error bars, were extracted at -350 mV. Note that after cleaning to 900 mV, the  $n_{\text{eff}}$  values for G6-NH<sub>2</sub>(Au<sub>147</sub>) and G6-NH<sub>2</sub>(Au<sub>55</sub>) overlap exactly.

is the same  $n_{\text{eff}}$  value observed after cleaning G6-NH<sub>2</sub>(Au<sub>147</sub>) DENs. In conjunction with the TEM and EXAFS results, which show that G6-NH<sub>2</sub>(Au<sub>147</sub>) and G6-NH<sub>2</sub>(Au<sub>55</sub>) DENs grow to be approximately the same size after three cleaning scans, the RRDE analysis also indicates a corresponding convergence of  $n_{\text{eff}}$  values for both sizes of DENs after cleaning scans. The key point is that the physical characterization data are fully consistent with the electrocatalysis results.<sup>[25,28,38,39,41,81]</sup>

### 2.7. Proposed Mechanism of NP Growth during Cleaning Scans

NP growth usually occurs via either Smoluchowski or Ostwald ripening. During Smoluchowski ripening, two or more NPs combine via aggregation or coalescence, forming larger NPs.<sup>[83,84]</sup> During the Ostwald ripening process, smaller and less stable NPs oxidize into soluble ions, which can then diffuse through solution before reducing onto the surface of larger, more stable NPs.<sup>[7,8,60,85]</sup>

To investigate the possibility of Smoluchowski ripening, cleaning scans were carried out using higher-generation G8-NH<sub>2</sub>(Au<sub>55</sub>) DENs. Previous studies have shown that higher-generation dendrimers having increased steric hindrance at their peripheries can suppress aggregation of Au<sub>147</sub> DENs during catalysis experiments.<sup>[25,86]</sup> Therefore, the hypothesis was that if Smoluchowski ripening is operative, it would be slowed by the larger dendrimers.

Figure S12 shows that after cleaning scans to 900 mV in N<sub>2</sub>-saturated, 0.10 M HClO<sub>4</sub>, the volume-weighted diameter for G8-NH<sub>2</sub>(Au<sub>55</sub>) DENs is 2.1 ± 0.3 nm. This size is similar to that observed for G6-NH<sub>2</sub>(Au<sub>55</sub>) DENs (Figure 3, 2.2 ± 0.5 nm), suggesting that increased steric hindrance at the periphery of the dendrimer does not affect the growth mechanism. This suggests that Smoluchowski ripening, if present, is less consequential than Ostwald ripening.

The literature also supports the hypothesis that AuNPs in the size range of 1–2 nm experience growth through Ostwald ripening. Specifically, AuNPs in the 1–2 nm size range undergo some oxidation to soluble Au ions rather than exclusively a surface oxide.<sup>[7,8,57,58]</sup> Indeed, it has been shown that polycrystalline Au can undergo potential-dependent anodic dissolution via a variety of mechanisms under acidic conditions, especially for electrodes having a high roughness factor.<sup>[23,57,58,87]</sup> There is evidence from both theory and experiment that this dissolution is more pronounced for AuNPs smaller than 1.5 nm.<sup>[4,7,8,24,60,61,88]</sup>

The foregoing literature studies of Au dissolution at positive potentials are directly relevant to our interpretation of the results in the present study. Specifically, we propose that when the electrode potential is scanned in the positive direction, AuNPs having sizes at the low end of the distributions shown in Figures 2 and 3 form soluble Au species rather than an insoluble oxide.<sup>[60]</sup> Upon reversal of the potential sweep, these soluble Au ions electrodeposit onto the surface of the larger, more stable AuNPs at the high end of the distributions.<sup>[8]</sup> The change in shapes of the size-distribution histograms in Figures 2 and 3, specifically the increase in tailing as the scan reversal potential is increased, are consistent with this mechanism.<sup>[62,63]</sup>

## 3. Summary and Conclusions

In this report, we have shown that just three electrochemical cleaning scans to modest positive potentials result in substantial growth of G6-NH<sub>2</sub>(Au<sub>55</sub>) DENs. Indeed, *ex-situ* TEM and *in-situ* XAS results indicate that G6-NH<sub>2</sub>(Au<sub>55</sub>) DENs grow to a limiting size of at least ~2 nm after just three cleaning scans. This size is the same as the G6-NH<sub>2</sub>(Au<sub>147</sub>) DENs. Importantly, this growth occurs prior to the onset of detectable faradaic Au oxidation or reduction. Accordingly, it is apparent that even minimal electrochemical cleaning significantly alters the size of 1–2 nm AuNPs.

The observed AuNP growth arising from electrochemical cleaning correlates to changes in the electrocatalytic ORR measurements. When G6-NH<sub>2</sub>(Au<sub>55</sub>) DENs undergo cleaning at potentials up to 900 mV, a significant suppression of the ORR kinetics is observed. Additionally, the  $n_{\text{eff}}$  values measured for G6-NH<sub>2</sub>(Au<sub>55</sub>) DENs following cleaning systematically increase and converge with the values recorded for G6-NH<sub>2</sub>(Au<sub>147</sub>) DENs. The key point is that after just three cleaning scans, and possibly after just one, the G6-NH<sub>2</sub>(Au<sub>147</sub>) and G6-NH<sub>2</sub>(Au<sub>55</sub>) DENs are essentially indistinguishable from both a physical characterization perspective and on the basis of their electrocatalytic properties.

The findings reported here have important implications for future studies of 1–2 nm AuNPs. Methods for synthesizing and characterizing NPs are becoming increasingly refined, and the results of this study highlight that it is important to characterize NPs not just after synthesis, but also following (or during) electrochemical cleaning and electrocatalysis. Accurate correlation of NP size and structure to catalytic activity will lead to a better understanding of the relationship between these parameters, thereby informing catalyst design and supporting robust theoretical calculations.<sup>[28]</sup>

## Acknowledgments

RMC gratefully acknowledges support from the Chemical Sciences, Geosciences, and Biosciences Division, Office of Basic Energy Sciences, Office of Science, U.S. Department of Energy (Contract: DE-SC0010576). RMC also thanks the Robert A. Welch Foundation (Grant F-0032) for sustained support. XAS analysis by AIF was supported by the National Science Foundation under Grant No. CHE-1903576. JL was supported in part by the U.S. Department of Energy, Office of Science, Office of Workforce Development for Teachers and Scientists (WDTS) under the Visiting Faculty Program (VFP). This research used beamline 7-BM (QAS) of the National Synchrotron Light Source II, a U.S. DOE Office of Science User Facility operated for the DOE Office of Science by Brookhaven National Laboratory (BNL) under Contract No. DE-SC0012704. The QAS beamline operations were supported in part by the Synchrotron Catalysis Consortium (U.S. DOE, Office of Basic Energy Sciences, grant number DE-SC0012335).

## Conflict of Interest

The authors declare no conflict of interest.

**Keywords:** electrocatalysis · nanoparticles · Ostwald ripening · oxygen reduction reaction · X-ray absorption spectroscopy.

- [1] J. H. Shim, J. Kim, C. Lee, Y. Lee, *J. Phys. Chem. C* **2011**, *115*, 305–309.
- [2] G. Gotti, D. Evrard, K. Fajerwerger, P. Gros, *J. Solid State Electrochem.* **2016**, *20*, 1539–1550.
- [3] J. H. Shim, J. Kim, A. Go, C. Lee, Y. Lee, *Mater. Lett.* **2013**, *91*, 330–333.
- [4] Y. Wang, E. Laborda, A. Crossley, R. G. Compton, *Phys. Chem. Chem. Phys.* **2013**, *15*, 3133–3136.
- [5] M. A. Montiel, F. J. Vidal-Iglesias, V. Montiel, J. Solla-Gullón, *Curr. Opin. Electrochem.* **2017**, *1*, 34–39.
- [6] N. Ostojic, Z. Duan, A. Galyamova, G. Henkelman, R. M. Crooks, *J. Am. Chem. Soc.* **2018**, *140*, 13775–13785.
- [7] M. Smiljanić, U. Petek, M. Bele, F. Ruiz-Zepeda, M. Sala, P. Jovanović, M. Gaberšček, N. Hodnik, *J. Phys. Chem. C* **2021**, *125*, 635–647.
- [8] B. P. Mainali, D. K. Pattadar, F. P. Zamborini, *J. Electrochem. Soc.* **2020**, *167*, 146503.
- [9] Y. Wang, J. Kim, *Electroanalysis* **2019**, *31*, 1026–1033.
- [10] S. L. Young, J. E. Kellon, J. E. Hutchison, *J. Am. Chem. Soc.* **2016**, *138*, 13975–13984.
- [11] E. Gervais, Y. Aceta, P. Gros, D. Evrard, *Electrochim. Acta* **2018**, *261*, 346–355.
- [12] L. M. Rossi, J. L. Fiorio, M. A. S. Garcia, C. P. Ferraz, *Dalton Trans.* **2018**, *47*, 5889–5915.
- [13] X. Tuae, S. Rudi, V. Petkov, A. Hoell, P. Strasser, *ACS Nano* **2013**, *7*, 5666–5674.
- [14] W. Hong, C. W. Li, *ACS Appl. Mater. Interfaces* **2019**, *11*, 30977–30986.
- [15] G. E. Ramirez-Caballero, Y. Ma, R. Callejas-Tovar, P. B. Balbuena, *Phys. Chem. Chem. Phys.* **2010**, *12*, 2209–2218.
- [16] C. Cui, M. Ahmadi, F. Behafarid, L. Gan, M. Neumann, M. Heggen, B. Roldan Cuenya, P. Strasser, *Faraday Discuss.* **2013**, *162*, 91–112.
- [17] Y. Wang, Y. Sun, H. Liao, S. Sun, S. Li, J. W. Ager III, Z. J. Xu, *Electrochim. Acta* **2016**, *209*, 440–447.
- [18] R. Devivaraprasad, N. Nalajala, B. Bera, M. Neergat, *Front. Chem.* **2019**, *7*, 648.
- [19] P. Saha, J. W. Hill, J. D. Walmsley, C. M. Hill, *Anal. Chem.* **2018**, *90*, 12832–12839.
- [20] J. Zhang, K. Sasaki, E. Sutter, R. R. Adzic, *Science* **2007**, *315*, 220–222.
- [21] E. Pizzutilo, S. J. Freakley, S. Geiger, C. Baldizzone, A. Mingers, G. J. Hutchings, K. J. J. Mayrhofer, S. Cherevko, *Catal. Sci. Technol.* **2017**, *7*, 1848–1856.
- [22] S. Koh, P. Strasser, *J. Am. Chem. Soc.* **2007**, *129*, 12624–12625.
- [23] J. Chinnaiha, O. Kasian, A. Dekshinamoorthy, S. Vijayaraghavan, K. J. J. Mayrhofer, S. Cherevko, F. Scholz, *ChemElectroChem* **2021**, *8*, 1524–1530.
- [24] J. T. Steven, V. B. Golovko, B. Johannessen, A. T. Marshall, *Electrochim. Acta* **2016**, *187*, 593–604.
- [25] J. A. Trindell, J. Clausmeyer, R. M. Crooks, *J. Am. Chem. Soc.* **2017**, *139*, 16161–16167.
- [26] Y. He, J.-C. Liu, L. Luo, Y.-G. Wang, J. Zhu, Y. Du, J. Li, S. X. Mao, C. Wang, *Proc. Nat. Acad. Sci.* **2018**, *115*, 7700–7705.
- [27] D. K. Pattadar, F. P. Zamborini, *J. Am. Chem. Soc.* **2018**, *140*, 14126–14133.
- [28] J. A. Trindell, Z. Duan, G. Henkelman, R. M. Crooks, *Chem. Rev.* **2020**, *120*, 814–850.
- [29] H. Li, L. Li, A. Pedersen, Y. Gao, N. Khetrapal, H. Jónsson, X. C. Zeng, *Nano Lett.* **2015**, *15*, 682–688.
- [30] P. Carro, E. Pensa, T. Albrecht, R. C. Salvarezza, *J. Phys. Chem. C* **2020**, *124*, 5452–5459.
- [31] R. Jin, C. Zeng, M. Zhou, Y. Chen, *Chem. Rev.* **2016**, *116*, 10346–10413.
- [32] Y. Luo, S. Fan, W. Yu, Z. Wu, D. A. Cullen, C. Liang, J. Shi, C. Su, *Adv. Mater.* **2018**, *30*, 1704576.
- [33] P. D. Jadzinsky, G. Calero, C. J. Ackerson, D. A. Bushnell, R. D. Kornberg, *Science* **2007**, *318*, 430–433.
- [34] M. R. Narouz, K. M. Osten, P. J. Unsworth, R. W. Y. Man, K. Salorinne, S. Takano, R. Tomihara, S. Kaappa, S. Malola, C.-T. Dinh, J. D. Padmos, K. Ayoo, P. J. Garrett, M. Nambo, J. H. Horton, E. H. Sargent, H. Hakkinen, T. Tsukuda, C. M. Crudden, *Nat. Chem.* **2019**, *11*, 419–425.
- [35] X. Kang, H. Chong, M. Zhu, *Nanoscale* **2018**, *10*, 10758–10834.
- [36] R. A. Masitas, F. P. Zamborini, *J. Am. Chem. Soc.* **2012**, *134*, 5014–5017.
- [37] O. S. Ivanova, F. P. Zamborini, *Anal. Chem.* **2010**, *82*, 5844–5850.
- [38] L. Sumner, N. A. Sakthivel, H. Schrock, K. Artyushkova, A. Dass, S. Chakraborty, *J. Phys. Chem. C* **2018**, *122*, 24809–24817.
- [39] W. Chen, S. Chen, *Angew. Chem.* **2009**, *121*, 4450–4453; *Angew. Chem. Int. Ed.* **2009**, *48*, 4386–4389.
- [40] T. Inasaki, S. Kobayashi, *Electrochim. Acta* **2009**, *54*, 4893–4897.
- [41] H. Mistry, R. Reske, Z. Zeng, Z.-J. Zhao, J. Greeley, P. Strasser, B. Roldan Cuenya, *J. Am. Chem. Soc.* **2014**, *136*, 16473–16476.
- [42] C.-Y. Lu, G. Henkelman, *J. Phys. Chem. Lett.* **2011**, *2*, 1237–1240.
- [43] D. R. Kauffman, D. Alfonso, C. Matranga, H. Qian, R. Jin, *J. Am. Chem. Soc.* **2012**, *134*, 10237–10243.
- [44] A. Bergmann, B. Roldan Cuenya, *ACS Catal.* **2019**, *9*, 10020–10043.
- [45] V. S. Myers, A. I. Frenkel, R. M. Crooks, *Langmuir* **2012**, *28*, 1596–1603.
- [46] S. Kabir, D. J. Myers, N. N. Kariuki, J. Park, G. Wang, A. Baker, N. Macauley, R. Mukundan, K. L. More, K. C. Neyerlin, *ACS Appl. Mater. Interfaces* **2019**, *11*, 45016–45030.
- [47] M. C. Smith, J. A. Gilbert, J. R. Mawdsley, S. Seifert, D. J. Myers, *J. Am. Chem. Soc.* **2008**, *130*, 8112–8113.
- [48] M. Povia, J. Herranz, T. Binninger, M. Nachttegaal, A. Diaz, J. Kohlbrecher, D. F. Abbott, B.-J. Kim, T. J. Schmidt, *ACS Catal.* **2018**, *8*, 7000–7015.
- [49] A. Chmielewski, J. Meng, B. Zhu, Y. Gao, H. Guesmi, H. Prunier, D. Alloyeau, G. Wang, C. Louis, L. Delannoy, P. Afanasiev, C. Ricolleau, J. Nelayah, *ACS Nano* **2019**, *13*, 2024–2033.
- [50] R. M. Crooks, M. Zhao, L. Sun, V. Chechik, L. K. Yeung, *Acc. Chem. Res.* **2001**, *34*, 181–190.
- [51] Y.-G. Kim, S.-K. Oh, R. M. Crooks, *Chem. Mater.* **2004**, *16*, 167–172.
- [52] V. S. Myers, M. G. Weir, E. V. Carino, D. F. Yancey, S. Pande, R. M. Crooks, *Chem. Sci.* **2011**, *2*, 1632–1646.

- [53] L. Zhang, R. M. Anderson, R. M. Crooks, G. Henkelman, *Surf. Sci.* **2015**, *640*, 65–72.
- [54] D. F. Yancey, L. Zhang, R. M. Crooks, G. Henkelman, *Chem. Sci.* **2012**, *3*, 1033–1040.
- [55] Y. Ju, H.-J. Ro, Y. Yi, T. Cho, S. Il Kim, C. W. Yoon, S. Jun, J. Kim, *Anal. Chem.* **2021**, *93*, 2871–2878.
- [56] A. S. Lapp, Z. Duan, N. Marcella, L. Luo, A. Genc, J. Ringnalda, A. I. Frenkel, G. Henkelman, R. M. Crooks, *J. Am. Chem. Soc.* **2018**, *140*, 6249–6259.
- [57] S. Cherevko, A. A. Topalov, A. R. Zeradjanin, I. Katsounaros, K. J. J. Mayrhofer, *RSC Adv.* **2013**, *3*, 16516–16527.
- [58] S. Cherevko, A. A. Topalov, I. Katsounaros, K. J. J. Mayrhofer, *Electrochem. Commun.* **2013**, *28*, 44–46.
- [59] L. D. Burke, P. F. Nugent, *Gold Bull.* **1997**, *30*, 43–53.
- [60] W. J. Plieth, *J. Phys. Chem.* **1982**, *86*, 3166–3170.
- [61] D. K. Pattadar, F. P. Zamborini, *Langmuir* **2019**, *35*, 16416–16426.
- [62] A. K. Datye, Q. Xu, K. C. Kharas, J. M. McCarty, *Catal. Today* **2006**, *111*, 59–67.
- [63] K. J. Hu, S. R. Plant, P. R. Ellis, C. M. Brown, P. T. Bishop, R. E. Palmer, *J. Am. Chem. Soc.* **2015**, *137*, 15161–15168.
- [64] P. Zhang, T. K. Sham, *Phys. Rev. Lett.* **2003**, *90*, 245502.
- [65] A. Jentys, *Phys. Chem. Chem. Phys.* **1999**, *1*, 4059–4063.
- [66] D. Glasner, A. I. Frenkel, in *AIP Conf. Proc.* (Eds.: B. Hedman, P. Pianetta), American Institute Of Physics, Stanford, **2007**, 746–748.
- [67] S. Eskandari, Y. Li, F. F. Tao, J. R. Regalbuto, *Catal. Today* **2019**, *334*, 187–192.
- [68] B. Roldan Cuenya, J. R. Croy, S. Mostafa, F. Behafarid, L. Li, Z. Zhang, J. C. Yang, Q. Wang, A. I. Frenkel, *J. Am. Chem. Soc.* **2010**, *132*, 8747–8756.
- [69] A. Frenkel, *Z. Krist.* **2007**, *222*, 605–611.
- [70] J. T. Miller, A. J. Kropf, Y. Zha, J. R. Regalbuto, L. Delannoy, C. Louis, E. Bus, J. A. van Bokhoven, *J. Catal.* **2006**, *240*, 222–234.
- [71] J. Wang, Q. Wang, X. Jiang, Z. Liu, W. Yang, A. I. Frenkel, *J. Phys. Chem. C* **2015**, *119*, 854–861.
- [72] W. Szczerba, H. Riesemeier, A. F. Thünemann, *Anal. Bioanal. Chem.* **2010**, *398*, 1967–1972.
- [73] M. Bron, *J. Electroanal. Chem.* **2008**, *624*, 64–68.
- [74] D. F. Yancey, E. V. Carino, R. M. Crooks, *J. Am. Chem. Soc.* **2010**, *132*, 10988–10989.
- [75] S. Guerin, B. E. Hayden, D. Pletcher, M. E. Rendall, J.-P. Suchsland, *J. Comb. Chem.* **2006**, *8*, 679–686.
- [76] S. Trasatti, O. A. Petri, *Pure Appl. Chem.* **1991**, *63*, 711–734.
- [77] D. Alba-Molina, A. R. P. Santiago, J. J. Giner-Casares, M. T. Martín-Romero, L. Camacho, R. Luque, M. Cano, *J. Phys. Chem. C* **2019**, *123*, 9807–9812.
- [78] A. J. Bard, L. R. Faulker, in *Electrochem. Methods Fundam. Appl.* (Eds.: D. Harris, E. Swain, C. Robey, E. Aiello), Elsevier, New York, **2001**, 87–136.
- [79] H. Erikson, A. Sarapuu, K. Tammeveski, J. Solla-Gullón, J. M. Feliu, *ChemElectroChem* **2014**, *1*, 1338–1347.
- [80] N. Alexeyeva, J. Kozlova, V. Sammelselg, P. Ritslaid, H. Mändar, K. Tammeveski, *Appl. Surf. Sci.* **2010**, *256*, 3040–3046.
- [81] H. Mistry, R. Reske, P. Strasser, B. Roldan Cuenya, *Catal. Today* **2017**, *288*, 30–36.
- [82] A. Galyamova, K. Shin, G. Henkelman, R. M. Crooks, *J. Phys. Chem. C* **2020**, *124*, 10045–10056.
- [83] Y. Fukamori, M. König, B. Yoon, B. Wang, F. Esch, U. Heiz, U. Landman, *ChemCatChem* **2013**, *5*, 3330–3341.
- [84] K. Manthiram, Y. Surendranath, A. P. Alivisatos, *J. Am. Chem. Soc.* **2014**, *136*, 7237–7240.
- [85] P. Dagtepe, V. Chikan, *J. Phys. Chem. C* **2010**, *114*, 16263–16269.
- [86] Y. Niu, L. K. Yeung, R. M. Crooks, *J. Am. Chem. Soc.* **2001**, *123*, 6840–6846.
- [87] S. Cherevko, A. R. Zeradjanin, G. P. Keeley, K. J. J. Mayrhofer, *J. Electrochem. Soc.* **2014**, *161*, 822–830.
- [88] H. Muto, K. Yamada, K. Miyajima, F. Mafuné, *J. Phys. Chem. C* **2007**, *111*, 17221–17226.

Manuscript received: April 22, 2021

Revised manuscript received: June 13, 2021